Nanoscale

COMMUNICATION

View Article Online
View Journal

Cite this: DOI: 10.1039/d6nr00425c

Received 31st January 2026,
Accepted 28th April 2026

DOI: 10.1039/d6nr00425c

rsc.li/nanoscale

Anchoring-group-controlled self-assembly and charge transport in antiaromatic molecular systems

Shintaro Fujii, *[a] Koshiro Isono,[b] Kazuki Nabeyama,[a] Ji-Young Shin, [b] Hiroshi Shinokubo *[b] and Tomoaki Nishino *[a]

Antiaromatic π-systems with 4*n* electrons are predicted to exhibit narrow frontier orbital gaps and enhanced charge-transport characteristics, but experimental studies at the single-molecule level have been limited by their intrinsic instability. Here, we investigate a chemically stable Ni(II) norcorrole (Ni(nor)) functionalized with thiol, pyridyl, and carboxyl anchoring groups using scanning tunnelling microscopy (STM) and single-molecule break-junction (BJ) measurements. STM imaging revealed distinct anchoring-group-dependent assemblies on the surface: thiol derivatives formed upright self-assembled monolayers, carboxylic acid derivatives produced one-dimensional supramolecular chains stabilised by intermolecular hydrogen bonding, whereas pyridyl derivatives did not form ordered structures on Au(111). These anchoring-dependent assemblies reflect variations in metal–molecule coupling and orbital alignment, leading to systematic modulation of charge-transport efficiency. Together, these results highlight anchoring-group chemistry as the primary design parameter governing metal–molecule coupling, surface assembly, and charge transport in molecular junctions. In this context, the antiaromatic Ni(II) norcorrole core serves as an electronic platform that provides intrinsically high conductance relative to aromatic analogues, while the anchoring groups determine the extent of conductance modulation and assembly behaviour. This distinction clarifies that antiaromaticity establishes a favourable electronic baseline, rather than acting as a unique driver of anchoring-dependent trends, and underscores the importance of anchoring chemistry for molecular device design.

Introduction

Aromaticity[1–3] and antiaromaticity[4,5] are fundamental concepts for describing the stability and electronic structure of cyclic π-conjugated molecules. According to Hückel's rule, planar cyclic systems with $4n + 2$ π electrons exhibit aromatic stabilisation, whereas those with $4n$ π electrons display antiaromatic character.[6] While aromatic molecules such as benzene are ubiquitous and chemically stable, antiaromatic compounds are generally destabilised by small frontier orbital gaps or partially filled orbitals, resulting in high reactivity and synthetic challenges. Nevertheless, antiaromatic π-systems are predicted to exhibit unique physical properties,[7–14] including narrow HOMO–LUMO gaps, multi-redox activity, and enhanced charge-transport characteristics, making them promising candidates for functional components in molecular electronics. However, understanding how these electronic features can be harnessed through controlled self-assembly processes remains unexplored.

The development of chemically stable antiaromatic species has enabled systematic investigations into these properties. In particular, the Ni(II) norcorrole (Ni(nor)) complex, the smallest antiaromatic porphyrinoid, can be synthesised on the gram scale and exhibits pronounced antiaromaticity with a closed-shell electronic structure.[15] This compound provides an ideal platform to explore the relationship between antiaromaticity and charge transport at the single-molecule level.[11] Previous studies have shown that antiaromatic Ni(nor) junctions display significantly higher conductance than that of the corresponding aromatic porphyrin analogue, consistent with reduced energy gaps and frontier orbital levels aligned closer to the Fermi energy levels of the electrodes.

In molecular junctions, charge transport is strongly influenced by the electronic structure of the molecule and the chemical nature of the anchoring groups that couple the molecule to metal electrodes.[16–20] Systematic studies on various anchoring moieties have demonstrated that contact resistance and level alignment are highly sensitive to functional groups such as thiol, pyridyl, and carboxyl.[17] Furthermore, substrate–anchoring interactions and intermolecular forces among anchoring groups, particularly hydrogen bonding,[21–25] can direct molecular assembly on metal surfaces, leading to the formation of ordered monolayers and supramolecular assemblies.

[a]Department of Chemistry, School of Science, Institute of Science Tokyo, 2-12-1 W4-10 Ookayama, Meguro-ku, Tokyo 152-8551, Japan. E-mail: fujii.s.e8cc@m.isct.ac.jp, tnishino@chem.titech.ac.jp
[b]Department of Applied Chemistry, Graduate School of Engineering, Nagoya University, Aichi, 464-8603, Japan. E-mail: hshino@apchem.nagoya-u.ac.jp

Despite these advances, a comprehensive understanding of how antiaromatic π-systems can be harnessed to control both surface assemblies and charge transport, particularly through the choice of anchoring groups, has not yet been achieved. It is crucial to develop anchoring-group-based strategies to exploit antiaromaticity for molecular device design. In particular, controlling self-assembly *via* anchoring-group interactions provides a useful structural context for understanding how anchoring chemistry influences metal–molecule coupling and charge-transport characteristics in molecular junctions bearing an antiaromatic π-system. In this work, we investigate Ni(nor) derivatives with different anchoring groups, combining scanning tunnelling microscopy (STM) and single-molecule break-junction (BJ) measurements.[16] We demonstrate that antiaromatic Ni(nor) forms anchor-dependent surface assemblies on Au(111), including self-assembled monolayers (SAMs) and hydrogen-bond–stabilised one-dimensional chains, and exhibits single-molecule conductance values more than two orders of magnitude higher than its corresponding aromatic porphyrin analogue. Moreover, systematic tuning of anchoring groups allows modulation of conductance over three orders of magnitude. Building on our previous demonstration of enhanced charge transport in antiaromatic Ni(II) norcorrole junctions, this study focuses on a systematic comparison of anchoring-group effects within a common antiaromatic molecular framework. Rather than introducing a new transport mechanism, the present work aims to clarify how established anchoring chemistries modulate surface assembly and metal–molecule coupling in an antiaromatic platform, providing a quantitative and internally consistent experimental benchmark.

Methods section

Materials and sample preparation

Ni(nor) derivatives with different anchoring groups (thiol, pyridyl, and carboxyl) and the reference aromatic Ni(II) porphyrin derivative with thiol anchoring groups (**1–3**, Fig. 1) were synthesized according to reported[11] or analogous procedures (SI 1 and Fig. S1–S3). For STM imaging and BJ experiments, A gold (Au) wire (Nilaco; 0.3 mm diameter, >99.9% purity) was mechanically cut to fabricate STM tips. Au(111) substrates were prepared by thermal evaporation of Au (>99.9%) onto mica. Samples were prepared by immersion of a Au substrate in a dichloromethane or toluene solution (0.1–0.5 mM) of **1–4** for more than 1 hour. After immersion, the substrate was washed with pure solvent and dried under a flow of inert gas. For STM observation of compound **1**, the molecular solution was heated to *ca.* 80 °C to promote its self-assembly on the Au substrate.[26]

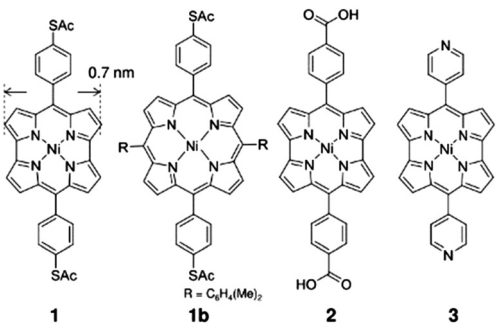

Fig. 1 Chemical structures of Ni(II) norcorrole derivatives (**1–3**) with different anchoring groups: thiol (protected as thioacetate, SAc), pyridyl, and carboxyl together with the aromatic Ni(II) porphyrin reference **1b** (thiol anchoring group also protected as thioacetate).

Scanning tunnelling microscopy measurements

STM experiments were performed using commercial scanning tunnelling microscopes under ultrahigh vacuum (JEOL JSPM-4500S)[27] or under ambient conditions (Bruker MS10). For surface-assembly characterisation, constant current topographic images were acquired at sample biases of 0.8–1.0 V and tunnelling currents of 0.1–0.3 nA (SI 2).

Single-molecule conductance measurements and analysis

Single-molecule conductance measurements were performed at room temperature using the STM setup equipped with an external piezoelectric driver (E-665, Physik Instrumente or M-2141, MESS-TEK) and a data acquisition device with LabVIEW 2018 (USB-6363 or PXI-4461, National Instruments). A Au STM tip was repeatedly brought into contact with and retracted from the Au(111) substrate at a bias voltage of 0.1–0.3 V (SI 3). During retraction, Au point contacts were ruptured to form nanoscale gaps that could be bridged by individual molecules. Thousands of conductance–distance traces during the retraction process were collected for each molecule and analysed statistically. It should be noted that single-molecule conductance measurements in this study were performed under both ultrahigh vacuum (UHV) and ambient conditions. Environmental factors such as surface adsorbates, junction stability, and electronic noise can influence the absolute conductance values obtained under different measurement environments. Accordingly, direct quantitative comparisons of conductance values are made only between measurements performed under the same environmental conditions. Importantly, despite these differences in measurement environment, the anchoring-group-dependent conductance trend remains consistent across both UHV and ambient experiments. In all cases, the conductance follows the order thiol > pyridyl > carboxyl, indicating that the relative conductance hierarchy is robust and primarily governed by anchoring-group-dependent metal–molecule coupling rather than by environmental factors.

Results and discussion

Anchoring-group-dependent surface assembly

The surface assemblies of Ni(nor) derivatives were first examined by STM on Au(111). For the thiol-anchored derivative (**1**),

bright protrusions corresponding to individual molecules were observed, suggesting the formation of upright SAMs stabilised by strong Au–S interactions. The STM image of the thiol-anchored derivative (**1**) (Fig. 2a) shows distributed dense bright protrusions with a nearest-neighbour spacing exceeding 0.5 nm, corresponding to upright-standing molecules (Fig. 2b and Fig. S4). In conventional alkanethiol SAMs on Au(111), molecules adopt the well-known $\sqrt{3} \times \sqrt{3}R30°$ adsorption structure with a lattice spacing of ~0.5 nm.[28] In contrast, the norcorrole framework of compound **1** has a lateral size exceeding 0.5 nm (Fig. 2 and Fig. S4),[29] and its steric bulk is incompatible with the ideal $\sqrt{3} \times \sqrt{3}R30°$ lattice. The resulting steric bulk and molecular anisotropy prevent the formation of a uniform, long-range ordered monolayer, accounting for the less homogeneous appearance of the observed films. In contrast, the carboxylic acid-terminated derivative (**2**) formed extended one-dimensional supramolecular chains on Au(111) terraces, oriented along the crystallographic directions of the substrate (Fig. 2c). The spacing between the molecular chains showed small variations of 1–3 nm, suggesting weak side-to-side intermolecular interactions. At the same time, higher-order commensurability with the Au(111) surface helps maintain the overall molecular orientation, supported primarily by tail-to-tail hydrogen bonding between terminal carboxyl groups, together with interactions with the Au(111) surface at room temperature. The formation of intermolecular hydrogen bonds between terminal carboxyl groups favours intermolecular association over direct Au–COOH binding. Such hydrogen-bond-directed supramolecular architectures are consistent with previous reports on dicyanoporphyrins on Au(111) at low temperature[21] and on dicarboxylic acid naphthalene derivatives on the more reactive Ag(110) at room temperature.[22] For small molecules such as terephthalic acid (TPA),[23–25] isolated one-dimensional chains are unstable and rapidly evolve into two-dimensional sheets because of weak molecule–substrate interactions and facile surface diffusion on Au(111) at room temperature.[23] In contrast, the carboxylic acid-functionalized Ni(nor) derivative affords well-defined linear supramolecular chains on Au(111) at room temperature. This difference can be rationalised by the cooperative effects of (i) strong tail-to-tail hydrogen bonding between the terminal carboxyl groups and (ii) the rigid, π-extended norcorrole core, which suppresses molecular diffusion and stabilises the linear arrangement on the Au surface at room temperature. These features explain why Ni(nor)–COOH derivatives form robust one-dimensional architectures at room temperature, whereas TPA molecules preferentially assemble into extended two-dimensional domains.

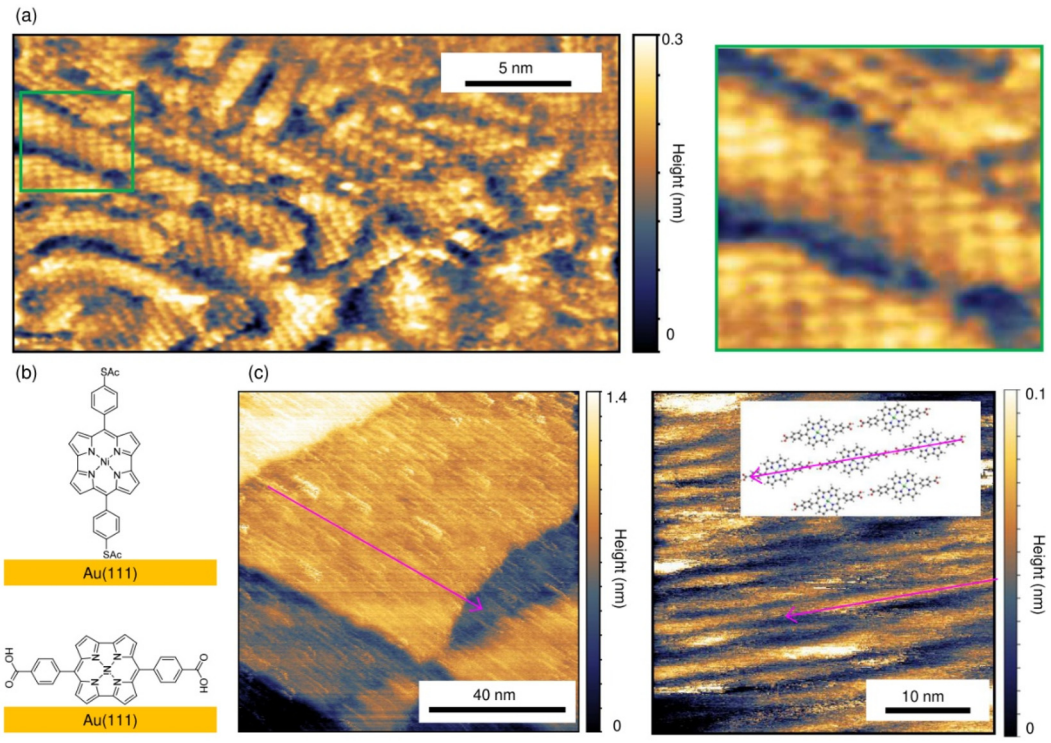

Fig. 2 Surface assemblies on Au(111). (a) STM image of thiol-anchored Ni(nor) (**1**) on Au(111) (sample bias voltage (V_s) = 1.0 V, tunnelling current (I_t) = 0.1 nA, scale bar = 5 nm). The right panel shows a magnified view of the area indicated by the square in the left image. (b) Schematic illustration of the adsorption geometries of **1** and **2**. (c) STM images of carboxyl-anchored Ni(nor) (**2**) on Au(111), displaying extended one-dimensional supramolecular chains stabilised by intermolecular hydrogen bonding (V_s = 0.8 V, I_t = 0.3 nA, scale bars = 40 nm (left) and 10 nm (right)). A proposed structural model of the one-dimensional supramolecular chains is shown in the inset of the left image. Arrows indicate the crystallographic directions along which the molecular chains are aligned. Note that different scale bars in (a) and (c) are used to emphasize the characteristic length scales of the respective assemblies; magnified views at comparable scales are included to facilitate structural comparison (Fig. S5).

The surface assemblies formed by compounds **1** and **2** are clearly distinguishable based on their characteristic structural motifs, although they occur on different length scales. As shown in Fig. 2a, the thiol-anchored derivative **1** forms densely packed, SAM-like features composed of localized protrusions, consistent with upright adsorption geometries stabilized by strong Au–S interactions. In contrast, the carboxyl-anchored derivative **2** forms extended one-dimensional supramolecular chains that propagate over tens of nanometres and align along the crystallographic directions of the Au(111) surface (Fig. 2c). Because these two assembly modes differ substantially in their characteristic length scales, the STM images are presented with different scale bars to optimally capture their representative features. To facilitate direct comparison, magnified views at comparable spatial scales are provided, highlighting the dense, isotropic packing of **1** in contrast to the anisotropic, linear motifs characteristic of the supramolecular chains formed by **2**.

By selecting the anchoring groups attached to the norcorrole core, the adsorption morphology can be systematically controlled, allowing the molecules to adopt either an upright or a parallel orientation on the surface (Fig. 2b). In contrast, molecules bearing pyridyl anchoring groups (**3**) did not form ordered assemblies under similar conditions, suggesting weaker interactions with the Au(111) substrate and less directional intermolecular interactions among neighbouring molecules (Fig. S6).

Single-molecule conductance

We next investigated how anchoring chemistry influences charge-transport properties using the STM-BJ method. In this technique, an Au tip is repeatedly brought into and retracted from contact with an Au(111) substrate in the presence of the target molecules. Upon rupture of the atomic-scale Au point contact, a nanometre-sized gap is formed between the tip and the substrate, which can be bridged by surface-adsorbed molecules to form single-molecule junctions. Fig. 3a and b presents a two-dimensional (2D) conductance–stretching-distance histogram constructed from thousands of conductance traces acquired under UHV conditions. In these measurements, the current through the molecular junctions was recorded at a fixed bias voltage during repeated stretching and breaking cycles. In the 2D histograms, the point at which the conductance dropped below $0.01G_0$ for **1**, **1b**, and **3**, and below $0.001G_0$ for **2** ($G_0 = 2e^2/h$), was defined as zero displacement, and the conductance traces were aligned accordingly. The statistical distribution observed in the 2D histogram thus reflects the most probable conductance values during the junction stretching. One-dimensional (1D) conductance histograms constructed from over 1000 traces revealed well-defined peaks (Fig. 3c). Remarkably, the conductance of Ni(nor) **1** reached $\sim 10^{-3}G_0$, more than two orders of magnitude higher than that of its aromatic analogue Ni(II) porphyrin **1b** ($\sim 10^{-5}G_0$) as reported previously under ambient conditions.[11] This result demonstrates that antiaromaticity can substantially enhance electron transport at the single-molecule level.

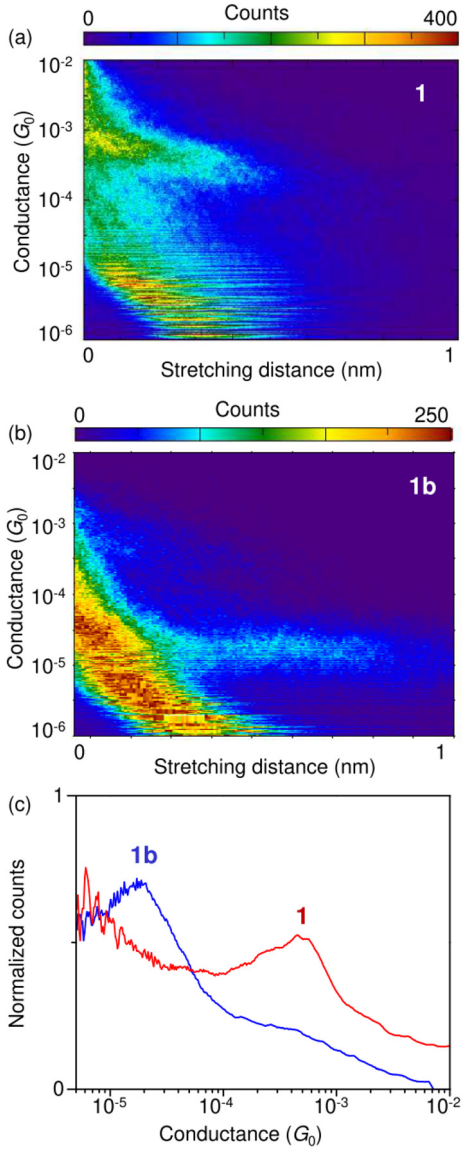

Fig. 3 (a and b) Two-dimensional (2D) histograms of conductance traces for (a) **1** and (b) **1b** at 0.1 V. (c) One-dimensional (1D) conductance histograms for **1** and **1b**. A total of 4000 and 2000 traces were used to construct the histograms for **1** and **1b**, respectively. The bin sizes for conductance [$\Delta\log(G/G_0)$] and stretching distance [$\Delta(\Delta d)$] were both set to 0.01. The horizontal features observed below approximately $1 \times 10^{-5}G_0$ arise from the finite current resolution of the data acquisition system, particularly in the UHV measurements where the signal approaches the detection limit of the measurement electronics. These features therefore represent instrumental artefacts and do not correspond to stable molecular junction configurations (SI 3).

To elucidate the role of metal–molecule coupling, we compared Ni(nor) derivatives with different anchoring groups. Fig. 4 shows 2D histograms of conductance traces for **2** and **3** under ambient conditions. Substitution with pyridyl reduced the conductance to $\sim 10^{-4}G_0$, while carboxyl anchoring further decreased it to $\sim 10^{-6}G_0$. In the 1D conductance histograms (Fig. 5), we compared the statistical conductance distributions of compounds **1–3**. While compound **2** did not exhibit a clear

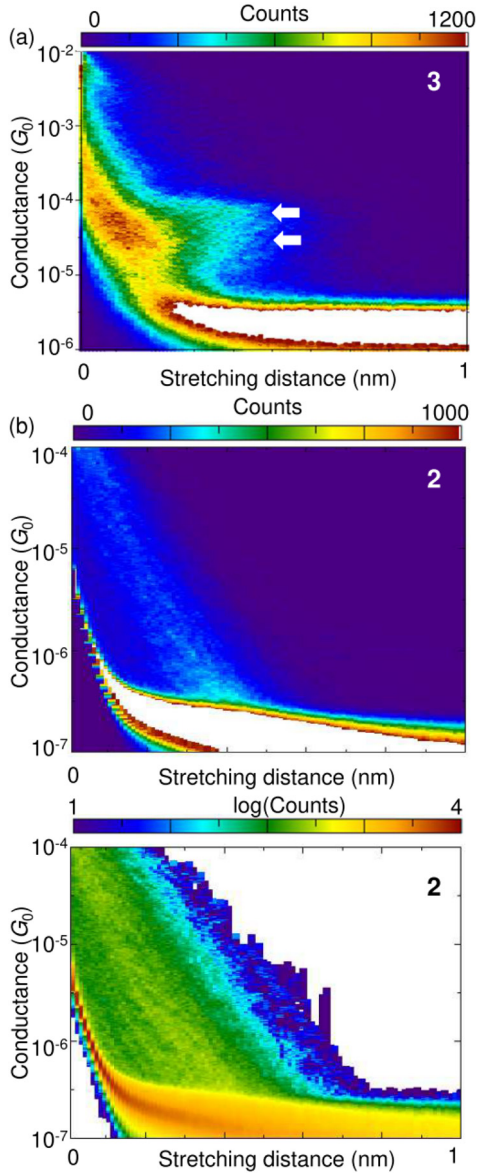

Fig. 4 2D histograms of conductance traces for (a) **3** and (b) **2** at 0.1 V and 0.3 V, respectively. Arrows in (a) indicate two conductance distributions arising from different metal–molecule interface structures (see main text for details). A total of 10 000 traces were used to construct each histogram. The bin sizes for conductance [$\Delta\log(G/G_0)$] and stretching distance [$\Delta(\Delta d)$] were both set to 0.01. For **2**, an additional 2D histogram plotted as log(counts) is also shown. The apparently coarser conductance resolution observed at higher bias (0.3 V) originates from the data acquisition settings required to accommodate increased current levels, rather than from an intrinsic change in molecular transport behaviour.

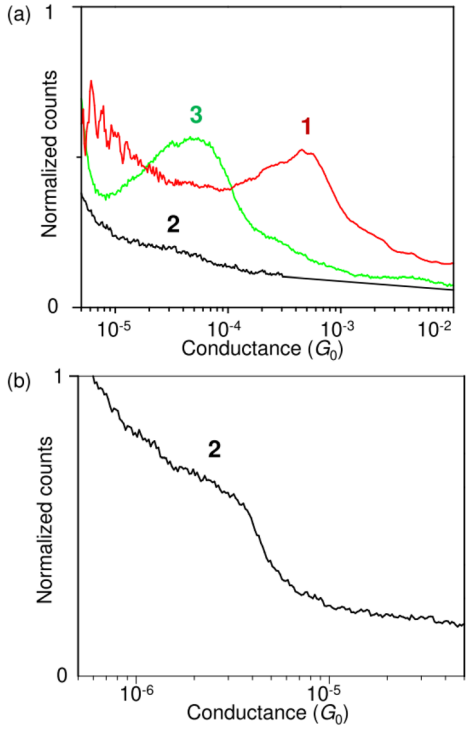

Fig. 5 Anchor-group-dependent conductance modulation. (a) 1D conductance histograms of Ni(nor) derivatives with thiol (**1**), carboxyl (**2**), and pyridyl (**3**) anchoring groups. (b) 1D conductance histogram of **2** in the low-conductance region. The bin size for conductance [$\Delta\log(G/G_0)$] is set to 0.01.

conductance peak, compounds **1** and **3** showed distinct peaks, with compound **1** displaying the higher conductance. It should be noted that pyridine-anchored molecular junctions are known to exhibit two conductance states depending on metal–molecule interface structure (see arrows in Fig. 4a),[30,31] which cannot be resolved in the present study (Fig. 5a). This is most likely due to the fact that the conductance values of the two states are close to each other. For the carboxyl-anchored derivative **2**, the conductance features appear close to the background tunnelling regime. As shown in the 2D conductance–distance histogram (Fig. 4b), adjustment of the colour scale improves the visibility of low-conductance features; however, no well-defined, extended molecular plateau is observed. Consistently, the corresponding 1D conductance histogram (Fig. 5) does not exhibit a clear conductance peak distinguishable from the background. Accordingly, we do not assign a definitive single-molecule conductance value to compound **2**. Instead, we note that its conductance lies near the detection limit under the present measurement conditions, which is consistent with very weak metal–molecule coupling associated with carboxyl anchoring. These observations indicate that the features observed for compound **2** should be interpreted cautiously and not overattributed to stable molecular junction configurations.

The observed trend for Ni(nor) derivatives can be attributed to differences in metal–molecule coupling. The Au–S interaction provides strong orbital overlap and efficient charge injection, whereas the coordinative Au–N (pyridyl) interaction is comparatively weaker. In the case of Au–COOH contacts,[17] the coupling is further reduced due to competing intermolecular hydrogen bonding under ambient conditions. The electronic coupling decreases in the order S > N (pyridyl) > COOH, resulting in a systematic reduction in conductance.

Variation of the anchoring chemistry modulates the single-molecule conductance over nearly three orders of magnitude. In our antiaromatic Ni(nor) junctions, the conductance follows the order S > N(pyridyl) > COOH, with $G_S/G_{N(pyridyl)} \approx 10$ and $G_S/G_{COOH} \approx 10^3$. These ratios are markedly larger than those reported for σ-type alkanes ($G_S/G_{N(amine)} \approx 20$–$70$, $G_S/G_{COOH} \approx 90$–370)[17] and π-conjugated systems ($G_S/G_{N(pyridyl)} \approx 4$–$60$).[20,32] Anchoring-group chemistry thus provides an effective means to control both interfacial coupling and charge-transport efficiency in molecular junctions based on antiaromatic cores.

Thiol anchoring provides strong Au–S coupling, thereby maximizing charge-injection efficiency. In contrast, carboxyl anchoring favours the formation of hydrogen-bonded chain structures but limits electronic coupling with the electrodes. Pyridyl anchoring affords intermediate conductance and weaker intermolecular cohesion, resulting in less ordered surface assemblies. Collectively, these findings indicate that anchoring-group chemistry plays a central role in defining both surface assemblies and charge-transport characteristics in antiaromatic Ni(nor) systems. In this context, surface organisation and conductance trends are correlated through their common dependence on anchoring chemistry, rather than implying a direct causal role of supramolecular interactions in charge transport.

Conclusions

In conclusion, we have systematically investigated how anchoring-group chemistry governs surface self-assembly and single-molecule charge transport in a series of Ni(II) norcorrole derivatives on Au electrodes. By combining STM-based structural characterization with statistically robust STM break-junction measurements, the present study allows a systematic comparison of binding geometry, assembly dimensionality, and transport efficiency within a common molecular framework. The results demonstrate that variations in anchoring groups primarily influence metal–molecule coupling and junction configuration, which in turn determine the observed conductance characteristics. While the norcorrole core provides a shared antiaromatic π-system, the experimental findings indicate that anchoring chemistry, rather than antiaromaticity itself or supramolecular interactions, plays the dominant role in shaping charge-transport behaviour in these molecular junctions. Taken together, this work provides a coherent experimental framework for understanding anchoring-group effects in molecular junctions based on antiaromatic π-systems, and offers a useful reference for the rational design and interpretation of single-molecule transport measurements in related systems.

Conflicts of interest

There are no conflicts to declare.

Data availability

The data supporting this article have been included as part of the supplementary information (SI). The supplementary information includes synthetic procedures, spectroscopic characterization, STM images, and additional experimental details. Supplementary information is available. See DOI: https://doi.org/10.1039/d6nr00425c.

Acknowledgements

This work was financially supported by JSPS KAKENHI (no. JP22H04974).

References

1 P. v. R. Schleyer, *Chem. Rev.*, 2001, **101**, 1115–1118.
2 G. Merino, M. Solà, I. Fernández, C. Foroutan-Nejad, P. Lazzeretti, G. Frenking, H. L. Anderson, D. Sundholm, F. P. Cossío, M. A. Petrukhina, J. Wu, J. I. Wu and A. Restrepo, *Chem. Sci.*, 2023, **14**, 5569–5576.
3 M. D. Peeks, *Adv. Phys. Org. Chem.*, 2024, **58**, 1–37.
4 R. Breslow, *Acc. Chem. Res.*, 1973, **6**, 393–398.
5 R. Lavendomme and M. Yamashina, *Chem. Sci.*, 2024, **15**, 18677–18697.
6 E. Hückel, *Z. Phys.*, 1931, **70**, 204–286.
7 N. Toriumi, A. Muranaka, E. Kayahara, S. Yamago and M. Uchiyama, *J. Am. Chem. Soc.*, 2015, **137**, 82–85.
8 M. Yamashina, Y. Tanaka, R. Lavendomme, T. K. Ronson, M. Pittelkow and J. R. Nitschke, *Nature*, 2019, **574**, 511–515.
9 Y. Ni, T. Y. Gopalakrishna, H. Phan, T. Kim, T. S. Herng, Y. Han, T. Tao, J. Ding, D. Kim and J. Wu, *Nat. Chem.*, 2020, **12**, 242–248.
10 D. Bradley, R. Tian, M. M. Bhadbhade, L. K. Macreadie, C. H. Sarowar and M. D. Peeks, *Inorg. Chem.*, 2024, **63**, 10103–10107.
11 S. Fujii, S. Marqués-González, J.-Y. Shin, H. Shinokubo, T. Masuda, T. Nishino, N. P. Arasu, H. Vázquez and M. Kiguchi, *Nat. Commun.*, 2017, **8**, 15984.
12 R. Nozawa, H. Tanaka, W.-Y. Cha, Y. Hong, I. Hisaki, S. Shimizu, J.-Y. Shin, T. Kowalczyk, S. Irle, D. Kim and H. Shinokubo, *Nat. Commun.*, 2016, **7**, 13620.
13 T. Ito, Y. Hayashi, S. Shimizu, J.-Y. Shin, N. Kobayashi, S. Ukai, A. Takamatsu, M. Nobuoka, Y. Tsutsui, N. Fukui, S. Ogi, S. Seki, S. Yamaguchi and H. Shinokubo, *Angew. Chem., Int. Ed.*, 2022, **61**, e202114230.
14 S. Kino, S. Ukai, N. Fukui, R. Haruki, R. Kumai, Q. Wang, S. Horike, Q. M. Phung, D. Sundholm and H. Shinokubo, *J. Am. Chem. Soc.*, 2024, **146**, 9311–9317.
15 T. Ito, Y. Hayashi, S. Shimizu, J.-Y. Shin, N. Kobayashi and H. Shinokubo, *Angew. Chem., Int. Ed.*, 2012, **51**, 8542–8545.
16 B. Xu and N. J. Tao, *Science*, 2003, **301**, 1221–1223.
17 F. Chen, X. Li, J. Hihath, Z. Huang and N. Tao, *J. Am. Chem. Soc.*, 2006, **128**, 15874–15881.

18 L. Venkataraman, J. E. Klare, I. W. Tam, C. Nuckolls, M. S. Hybertsen and M. L. Steigerwald, *Nano Lett.*, 2006, **6**, 458–462.
19 A. Mishchenko, L. A. Zotti, D. Vonlanthen, M. Bürkle, F. Pauly, J. C. Cuevas, M. Mayor and T. Wandlowski, *J. Am. Chem. Soc.*, 2011, **133**, 184–187.
20 V. Kaliginedi, A. V. Rudnev, P. Moreno-García, M. Baghernejad, C. Huang, W. Hong and T. Wandlowski, *Phys. Chem. Chem. Phys.*, 2014, **16**, 23529–23539.
21 T. Yokoyama, S. Yokoyama, T. Kamikado, Y. Okuno and S. Mashiko, *Nature*, 2001, **413**, 619–621.
22 J. Schnadt, E. Rauls, W. Xu, R. T. Vang, J. Knudsen, E. Lægsgaard, Z. Li, B. Hammer and F. Besenbacher, *Phys. Rev. Lett.*, 2008, **100**, 046103.
23 S. Clair, S. Pons, A. P. Seitsonen, H. Brune, K. Kern and J. V. Barth, *J. Phys. Chem. B*, 2004, **108**, 14585–14590.
24 J. D. Fuhr, A. Carrera, N. Murillo-Quirós, L. J. Cristina, A. Cossaro, A. Verdini, L. Floreano, J. E. Gayone and H. Ascolani, *J. Phys. Chem. C*, 2013, **117**, 1287–1296.
25 T. W. White, N. Martsinovich, A. Troisi and G. Costantini, *J. Phys. Chem. C*, 2018, **122**, 17954–17962.
26 M. I. Béthencourt, L. Srisombat, P. Chinwangso and T. R. Lee, *Langmuir*, 2009, **25**, 1265–1271.
27 S. Fujii, M. Ziatdinov, S. Higashibayashi, H. Sakurai and M. Kiguchi, *J. Am. Chem. Soc.*, 2016, **138**, 12142–12149.
28 J. C. Love, L. A. Estroff, J. K. Kriebel, R. G. Nuzzo and G. M. Whitesides, *Chem. Rev.*, 2005, **105**, 1103–1170.
29 R.-F. Dou, X.-C. Ma, L. Xi, H. L. Yip, K. Y. Wong, W. M. Lau, J.-F. Jia, Q.-K. Xue, W.-S. Yang, H. Ma and A. K.-Y. Jen, *Langmuir*, 2006, **22**, 3049–3056.
30 X.-S. Zhou, Z.-B. Chen, S.-H. Liu, S. Jin, L. Liu, H.-M. Zhang, Z.-X. Xie, Y.-B. Jiang and B.-W. Mao, *J. Phys. Chem. C*, 2008, **112**, 3935–3940.
31 S. Y. Quek, M. Kamenetska, M. L. Steigerwald, H. J. Choi, S. G. Louie, M. S. Hybertsen, J. B. Neaton and L. Venkataraman, *Nat. Nanotechnol.*, 2009, **4**, 230–234.
32 W. Hong, D. Z. Manrique, P. Moreno-García, M. Gulcur, A. Mishchenko, C. J. Lambert, M. R. Bryce and T. Wandlowski, *J. Am. Chem. Soc.*, 2012, **134**, 2292–2304.